Supplementary Data

Table of contents:

Item DR1. Laser Ablation Inductively Coupled Plasma Spectroscopy study of the coating on the albite grain characterized in this study by TEM and FIB

The trace-element composition of the coating on the albite grain (Fig. DR1-1) was measured by laser ablation inductively-coupled plasma mass spectrometry (LA-ICP-MS) using a New Wave Nd-YAG 213 nm laser coupled to a quadrupole Thermo X II mass spectrometer. Ablation was done in a He atmosphere and Ar was mixed to the carrier gas before it entered the ICP-MS. Line scans and maps were recorded with spot sizes of 10 and 3 μm, respectively, using a repetition rate of 10 Hz and an energy density of 11 Jcm^{-2}. The synthetic glass standard NIST610, which contains a nominal trace-element abundance of ~500 $mgkg^{-1}$ was used as the external standard. The standard was ablated under the same conditions at the beginning of each analytical run, intermittently during acquisition, and at the end of each sample. Detection limits for the individual elements and the quantification methodology are given in Durocher and Schindler (2011). Line scans were designed to traverse the cross-section of coated grains, moving from the surrounding epoxy (labelled *A* in Fig. DR1-1) and traveling through the coating toward the underlying mineral (labeled *B*). Integration areas were selected based on chemical differences between the coatings and matrix composition as obtained by SEM-EDS analyses.

Reference

Durocher, J. and Schindler, M. (2011): Iron-hydroxide, iron-sulfate and hydrous-silica coatings in acid-mine tailings facilities: A comparative study of their trace-element composition. *Applied Geochemistry* **26**, 1337-1352.

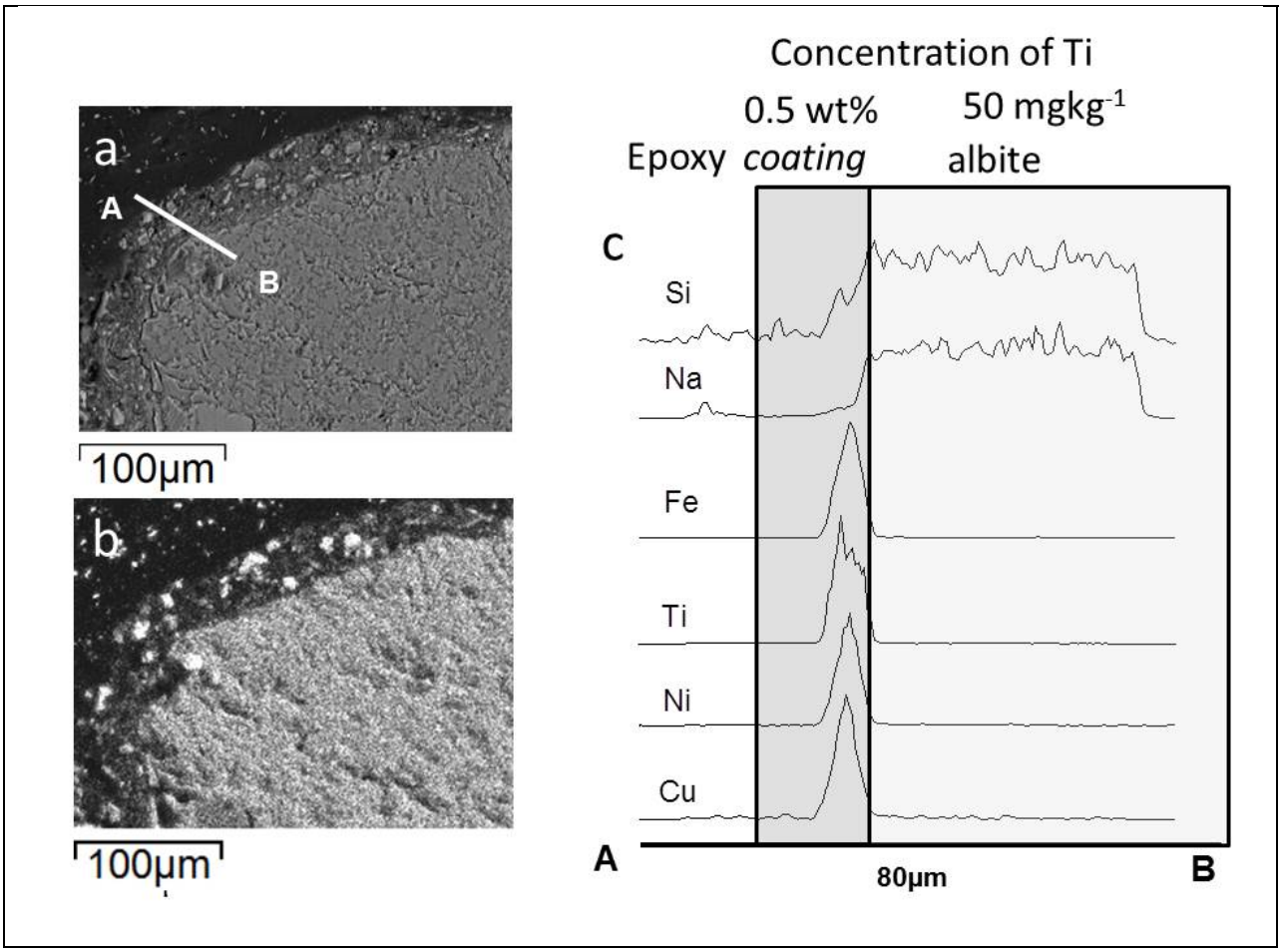

Figure DR1-1. a. BSE image of the coatings indicating the traverses of the Laser ablation ICP-MS line scans; b EDS chemical distribution map for Si in the coatings; c. Recorded pattern of Laser ablation ICP-MS line scans with the distance between A and B versus the intensity [CPS] for selected elements. Quantification of the data shows that Ti is enriched in the coatings by a factor 100 relative to the underlying albite.

Item DR2. Laser Ablation Inductively Coupled Plasma Spectroscopy study of Ti-bearing Particulate Matter emitted from the smelters in the Sudbury area.

The chemical distributions of trace elements in particulate matter emitted from the smelter and deposited onto soils of the Sudbury area were studied by Lanteigne et al. (2014). The sampling locations of the particulate matter were the same as for the coated mineral grains (see methodology section in text). Chemical distribution maps for selected elements including Al and Ti in a spherical particulate are shown in Figure DR2-1 and the average concentrations for Ti in different components within five spherical particulates are listed in Table DR2-1**.** The occurrence of distinct components in a spherical particulate can be recognized in Figure S2-1. The weathering of spherical smelter-derived particulates were studied by Lanteigne et al. (2012) (Figure DR2-2) and gave evidence for the release of metal(loids) including Ti into the upper soil horizons.

Table DR2-1. Average concentration of Al and Ti in five different spherical particulates and their components

Components	Al [wt%]	Ti [mgkg-1]
Average in the spheres	1.8	1200
Sulfide inclusion	1.0	800
Matrix	2.0	1500
Metal(loid)-rich rim	1.6	630

References

Lanteigne, S., Schindler, M., McDonald, A.M., Skeries, K., Abdu, Y., Mantha, N.M., Murayama, M., Hawthorne F.C. and Hochella, Jr, M.F. 2012, Mineralogy and weathering of smelter-derived spherical particles in soils: implications for the mobility of Ni and Cu in the surficial environment. Water, Air, & Soil Pollution 223, 3619-3641.

Lanteigne, S., Schindler, M. and McDonald, A. 2014, Distribution of metal(loid)s in smelter-derived particulate matter in soils, mineralogical insights into their retention and release in a low-T environment. Can. Mineral. 52, 453-471.

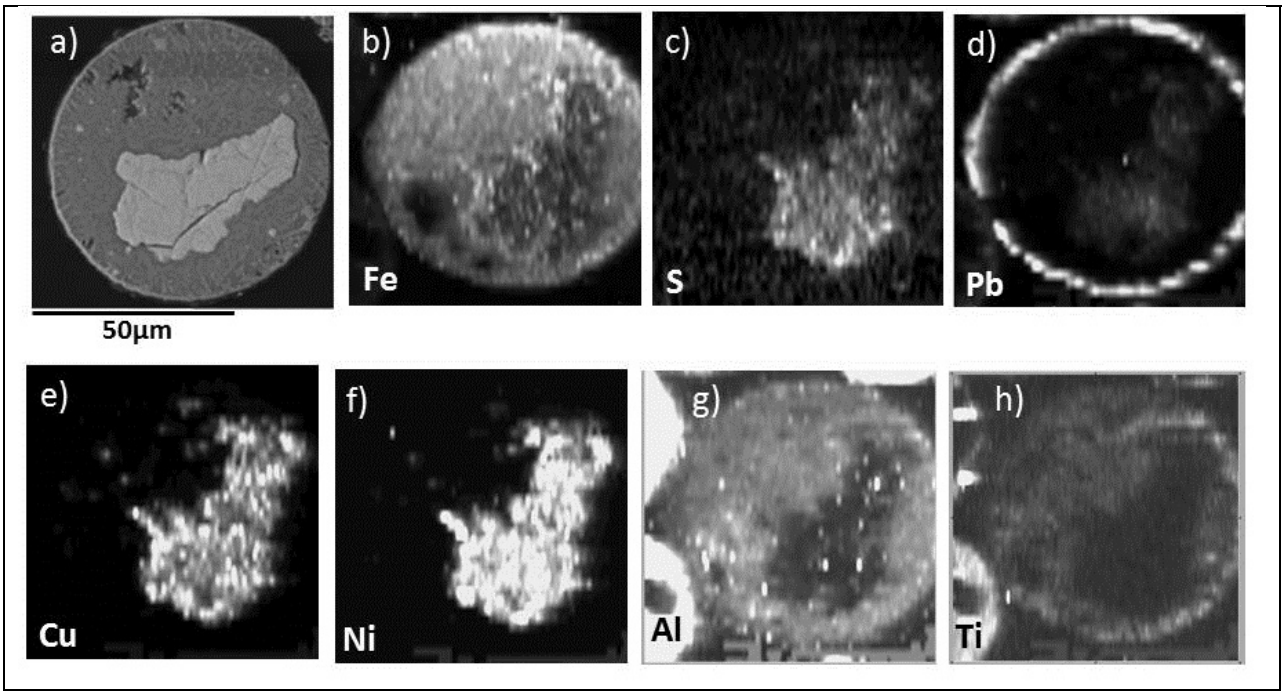

Figure DR2-1. (a)-(h). Laser-Ablation ICP-MS chemical distribution maps for selected elements in a spherical particulate including those of Ti (h). The presence of a sulfide-rich core, and a metal(loid)-rich rim can be recognized in the chemical distribution maps for S and Pb, respectively.

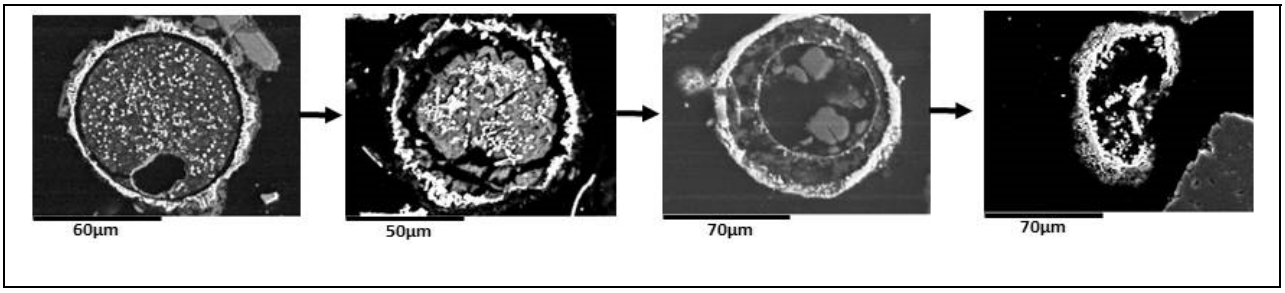

Figure DR2-2. Proposed weathering sequence of spherical smelter-derived particulates (modified from Lanteigne et al. 2014)

Item DR3. Study of snow samples below the smelter plume; evidence for the smelter emission of Ti and Zr-bearing particulate matter

Snow samples were collected under the smelter plume emitted from Vale's "Superstack", Copper Cliff, Sudbury, ON after three separate snow fall events (Table DR3-1). Snow samples were collected at intervals of circa 1 kilometre along 50 kilometres transects starting in the vicinity of Vale's "Superstack" following the direction of the primary wind that occurred during the snow fall event. Samples were taken a minimum of 5 meters from the road to ensure little interference from road dust and exhaustive emissions from automobiles. The snow samples were collected in 1 litre polyurethane containers from a 1 metre by 1 metre square, where only the top layer of snow was gathered. The containers were filled to their maximum capacity to ensure consistency.

Table DR3-1. Sampling of snow samples below the "Superstack" plume after snow fall event

Traverse	Date	Snow accumulation [cm]	Wind direction	Number of samples	Figure number of traverses and concentration profiles for Ti and Zt
A	November, 25th, 2014	4	South-West	45	S4A, S5A, S6A
B	November, 17th, 2014	6.6	South	39	S4B, S5B, S6B
C	January 18th, 2015	7.8	North West	43	S4C, S5C, S6C

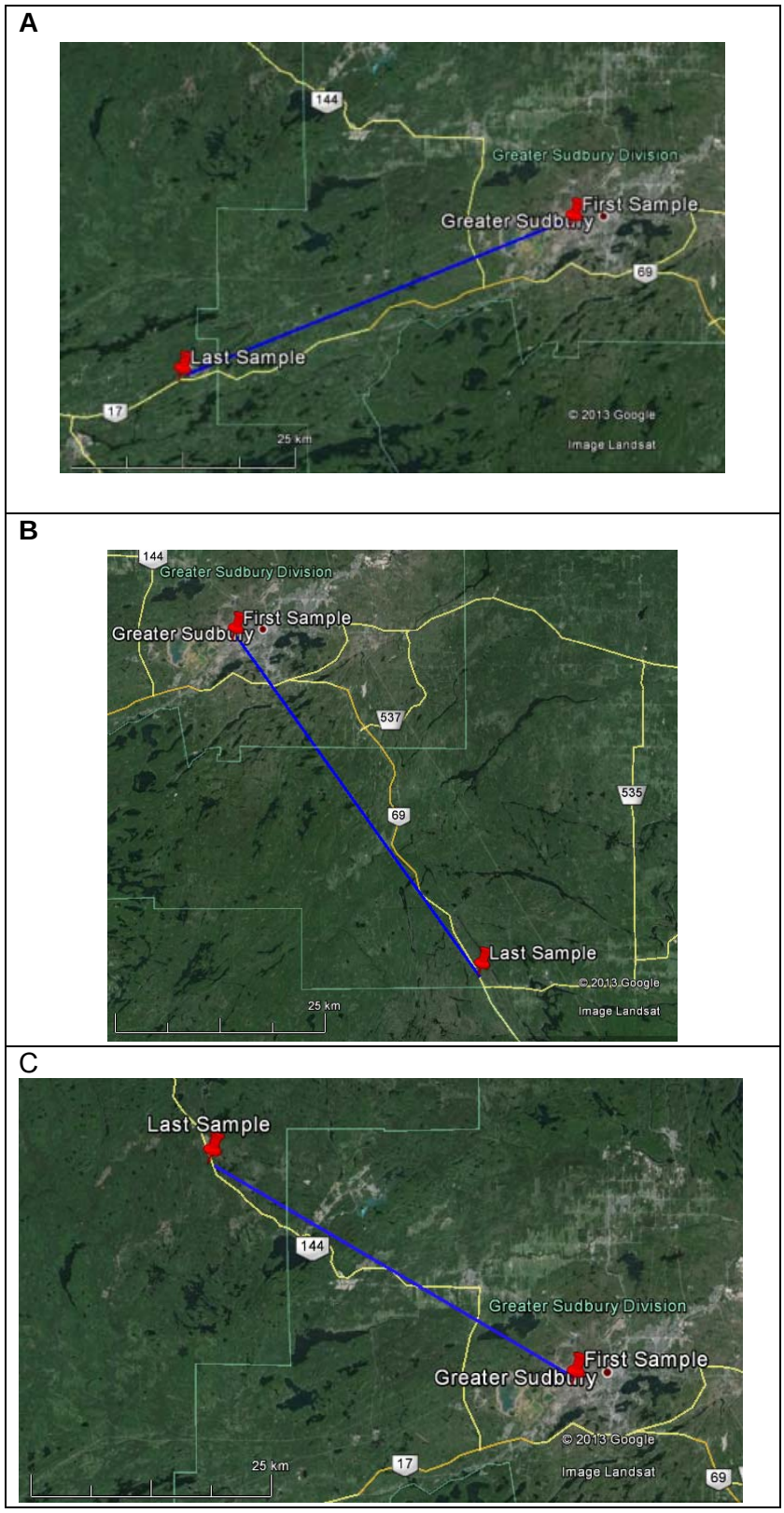

Figure DR3-1. Traverses A, B and C of the snow sampling events listed in Table DR2.

Elemental analysis

All samples were stored in a fridge at approximately 3ºC, with the corresponding weights of the liquids being recorded with a Mettler AE 260 Delta Range scale. Each sample was shaken vigorously, with 5ml or 7.5ml being immediately transferred into a 15ml Falcontube, reflecting snow density on sampling. Fifty ml of each sample were transferred into digestion tubes, heated at a temperature of 80ºC for 24-26 hour period to complete evaporation. The residues were dissolved in 7.5 mL HNO_3 and 2.5mL of HCl at 105ºC in closed digestion tubes, then evaporated near dryness prior to residue digestion at 50ºC with 2.5 mL of HNO_3, cooled and diluted to 15 mL final volume with distilled water. Concentrations of the elements were subsequently measured with a Varian 810 ICP-MS in high resolution mode. Accuracy and precision was ensured with the use of duplicates, reference materials and analytical spikes.

Results

Concentration profiles for Ti and Zr in snow samples collected along the traverses indicate an increase in the concentration of both elements with distance (Figures S3-2 and S3-3). Similar profiles in the distance range of 25-50 km were observed for Cu and Ni, the major elements in the smelted ore. These observations suggest that Ti and Zr have been deposited in the distance range of 25 to 50 km in the form of particulate matter with a similar size and density as Cu- and Ni-bearing particulate matter. Other factors that affected the deposition of Zr- and Ti-bearing particulate matter include (a) the shadow effect of the 380 m tall stack, (b) wind blowing in vertical directions and (c) density and amount of the snowfall event. During the peak of smelter emissions (1913-1972), particulate matter was emitted from much smaller stacks and without any filtering. Hence, a much larger amount of Zr and Ti-bearing particulate was most likely deposited in proximity to the stacks as it is now observed for the “Superstack”.

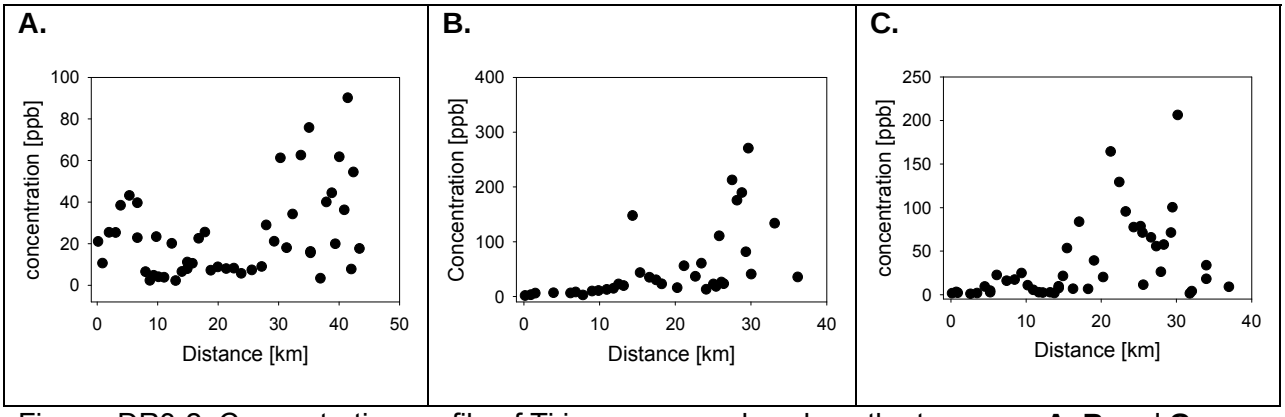

Figure DR3-2. Concentration profile of Ti in snow samples along the traverses **A**, **B** and **C** labelled A, B and C

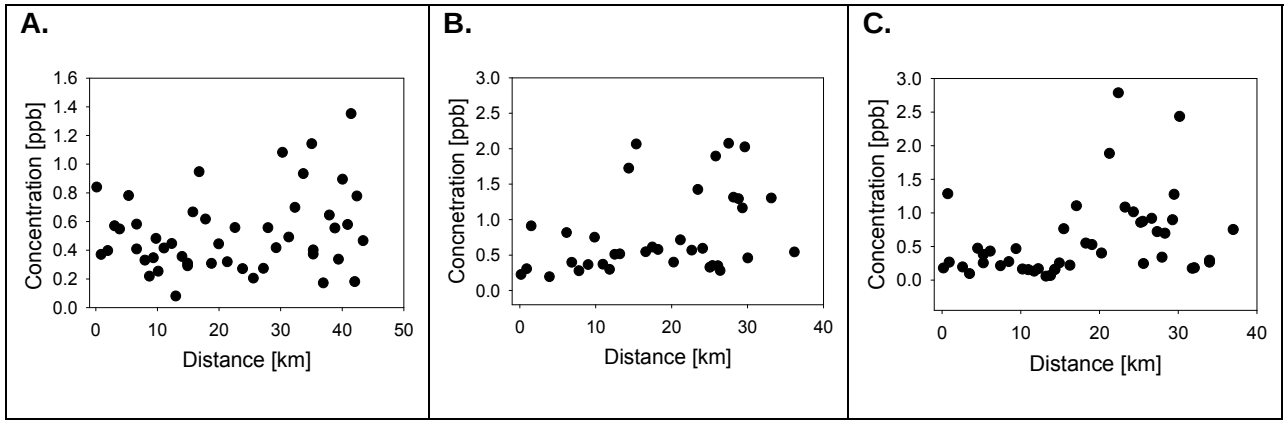

Figure DR3-3. Concentration profile of Zr in snow samples along the traverses **A**, **B** and **C** labelled A, B and C.

Item DR4. Study on the distribution of Zr and Ti in a profile through an acidic non-remediated soil profile; evidence for the higher proportion of Zr and Ti in the soluble (colloidal) fraction of soil horizons with lower pH

A soil profile was collected from inside the City of Greater Sudbury (Coordinates; N: 46°29'56.0", W: 80°58'20.2") (Fig. DR4-1a) by Driscoll (2013). This location is approximately 11km south west of the Falconbridge smelter (location of the sampling site of the mineral grain examined in this study), 10km west of the Coniston smelter, and 9km east of the Copper Cliff smelter, inside the semi-barren vegetation zone of Sudbury. This location was chosen because the area has never been impacted by the Sudbury re-greening processes such as liming as indicated by the low pH (3.7) of the organic horizon. Further, the surface horizons of the soils at this site are contaminated in the majority of the chemicals of concern outlined by previous studies. The predominant vegetation at the site was an old growth oak stand with little undergrowth and few other tree species in the area chosen for sample collection. The surrounding forest contained coniferous species in more rocky areas. The soils on this site are an admixture Orthic Dystric Brunisols in the poorly drained areas and an Orthic Humo-Ferric Podzol in the better drained areas. The actual pedon sampled was the Podzolic soil with a well-developed Ae horizon and deeper mineral Bf horizons (Fig. DR4-1b). In the fall of 2011, a soil pit (approximately $1m^2$ and 70cm deep) was dug in the area described above. Fresh litter was removed before the soil pit was dug. Individual soil horizons were manually excavated with a stainless steel spade and separated into clean five gallon buckets. The spade was cleaned in between horizon samples to minimize contamination. The Podzolic soil profile has well developed LFH, Ae, Bf and BC horizons overlying the parent till which was deposited on bedrock (Fig. DR4-1b).

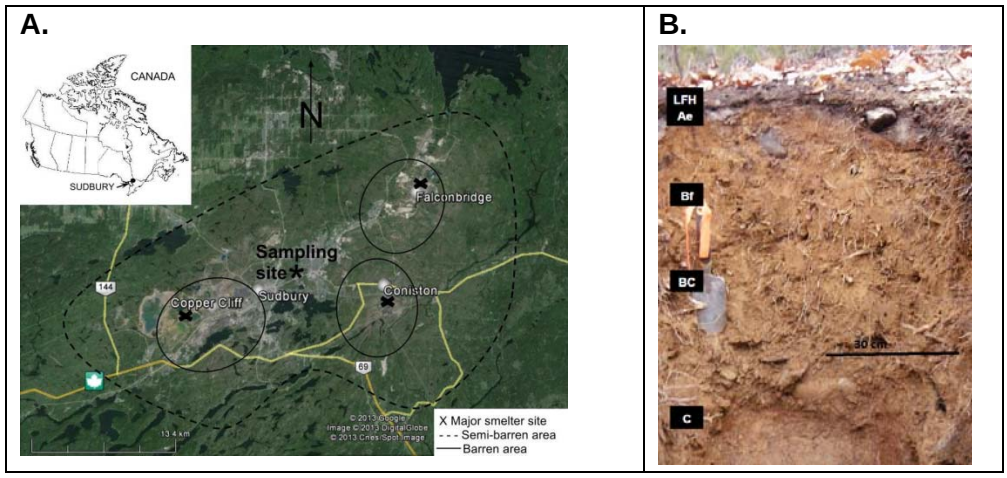

Figure DR4-1. A. Location of the sampling site and B. profile through the horizons LFH to C

Methodology

The soil was air dried at room temperature for two weeks before it was passed through a 2mm sieve using a Ro-Tap Shaker and homogenized. The organic horizon was sieved by hand to 6.25mm, with partially decomposed leaves and roots being lightly macerated to pass the sieve

mesh. Rocks or large living roots were discarded. Approximately one kilogram of each horizon was removed for further analysis. The pH of the soil samples was measured using a 1:2 soil to solution ratio (1:4 for organic LFH soils) in both deionised water and 0.01 M $CaCl_2$ (Thomas, 1996).The soluble fraction of a metal and metalloid content was determined by a $LiNO_3$ extraction. Five gram of mineral soil or 2 g of organic soil being weighed into 50mL centrifuge tubes into which 20 mL of a 0.01 M $LiNO_3$ solution was added and the samples being placed on a reciprocal shaker for 24 hours. Samples were then centrifuged and the supernatant filtered through a 0.45µm cellulose filter and diluted for analysis by ICP-MS.

Elemental analysis

A wide suite of metals and metalloids was quantified for each soil sample. The soil samples were oven dried for 24 hours at 105°C and lightly crushed by mortar and pestle to pass a 75 µm sieve. 0.2 g of soil was weighed into a 50 mL flat bottom tube (polypropylene), then 10 mL of 10:1 HF and HCl was added, and the mixture heated to 110°C for 210 minutes (or to dryness). This step was then repeated, after which 7.5 mL of HCl and 7.5 mL of HNO_3 were added to each tube and the mixtures heated to 110°C for 240 minutes until the samples were dry. In the final step, 0.5 mL of HF, 2 mL of HCl, and 10 mL of HNO_3 were added to the tubes, with heating to 110°C for 60 minutes to allow sample to dissolve and remain in solution. The resultant solutions were then diluted to 50 mL with deionised water, with a further factor of 10 dilution of a subsample before analysis by ICP-MS (Varian 810). The digestion was performed on a programmable digestion block (Questron Technologies Corp) and all acids were concentrated, trace metal grade (Fisher Scientific). Quality control analyses included a method blank, a duplicate sample, two spiked samples, and three certified reference materials (SU-1B, RTS-3a, and LKSD-1) every 15 real samples. An internal standard solution of Re and Ru (10 µg/L) was used to correct for mass bias and calibration drift.

Results

Depth profiles through non-remediated acidic soils display commonly larger variations in pH than remediated soils; i.e. with lower pH values in the upper than lower soil horizons (Fig. 4-2A). Hence, concentration profiles of Zr and Ti through a soil that has not been remediated gives a better understanding how the soluble (colloidal) fraction for both elements varies with the change in pH. The soluble fraction of an element is the fraction that occurs loosely bounded to mineral surfaces in form of colloids or adsorption complexes and that can be removed with an electrolyte solution (in this case $LiNO_3$). Figure 4-2A shows that the soluble fraction of Zr and Ti correlates with the acidity of the soil horizon but not with the total amount of each element in the horizon; i.e. the soluble fraction of an element is more controlled by the acidity of a soil horizon that by the total concentration of an element. The latter observation suggests that the acidification of the soils during the peak of smelting in the Sudbury area resulted in an increase in the proportions of Ti and Zr in the soluble fractions of the upper soil horizons in the Sudbury area.

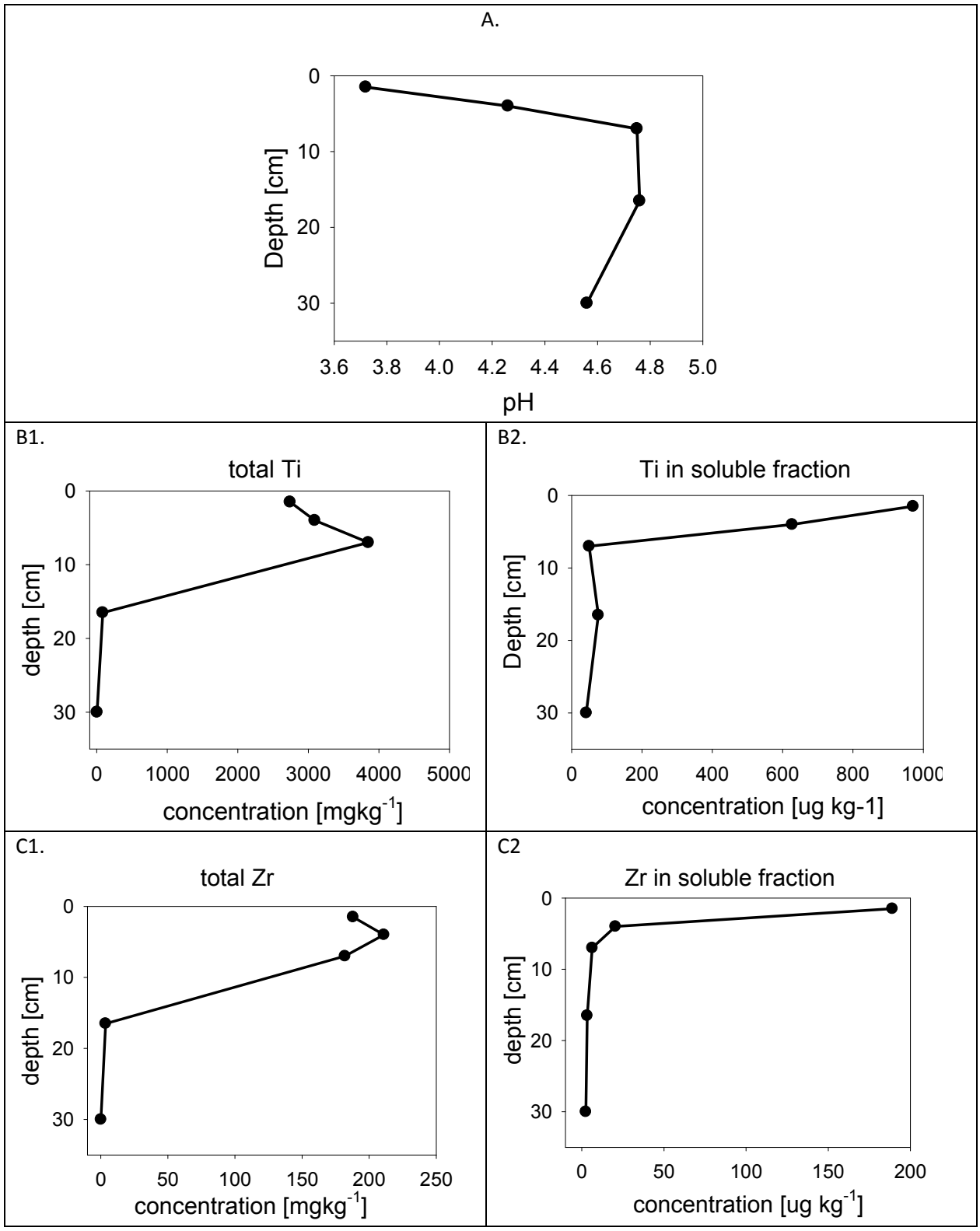

Figure DR4-2. A. pH versus depth; B1 and C1. total concentrations of Ti and Zr with depth, respectively; B2 and C2: concentrations of Ti and Zr in the soluble fractions of the soil horizons versus depth, respectively.

Item DR5. Selected area diffraction pattern of zircon and a Magneli phase and diffraction data of other phases.

Phases were identified on the basis of their chemical composition, selected area electron diffraction (SAED) pattern, the morphology of their grains and the spacing between lattice fringes in real space or in Fast Fourier Transformation (FFT) images. Large size SAED pattern are shown below for zircon (Fig. DR5-1) and the Magneli phase Ti_5O_9 (Fig. DR5-2). Diffraction pattern and the corresponding measured and observed d-spacing and indices are listed for all other phases in Table DR5-1.

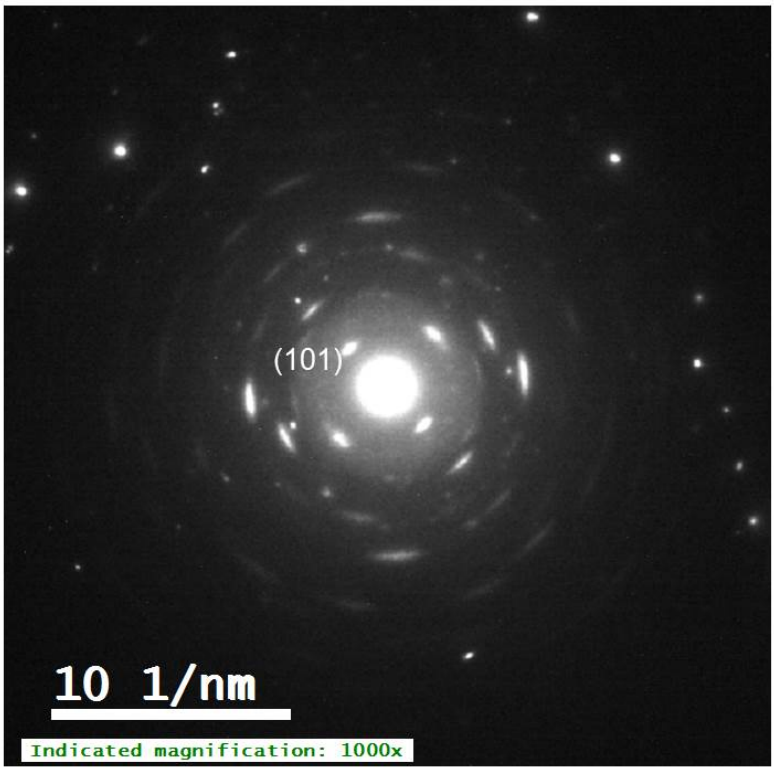

zircon

distances measured	d spacings	d spacings recorded	indices
4.492	4.452359751	4.43	101
9.016	2.218278616	2.2172	202
5.973	3.348401138	3.3	200
9.52	2.100840336	2.0667	301

Figure DR5-1. top: SAED pattern of zircon; the diffraction spot for the (101) plane is labelled; bottom: measured distances of diffraction spots to (000), calculated and recorded d-spacing (from the MSA crystallography data base) and indices of the corresponding lattice planes. Zircon could be easily identified on the d-spacing of the (101) plane with d= 4.42 Å.

A

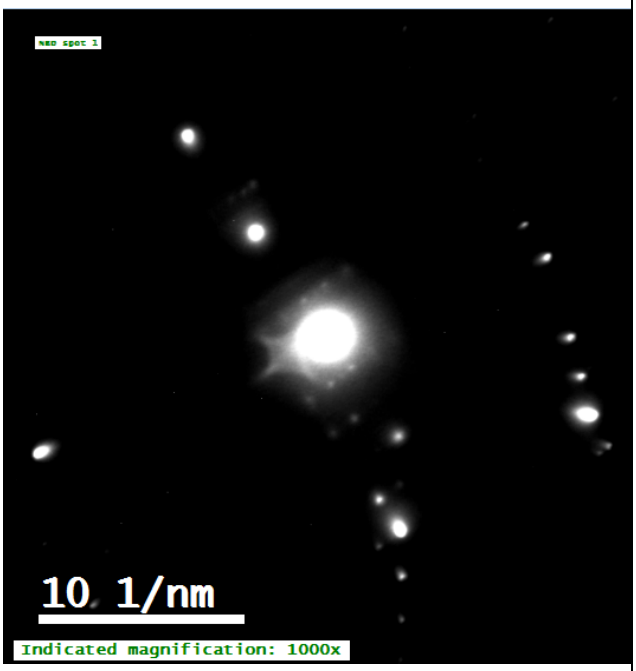

B

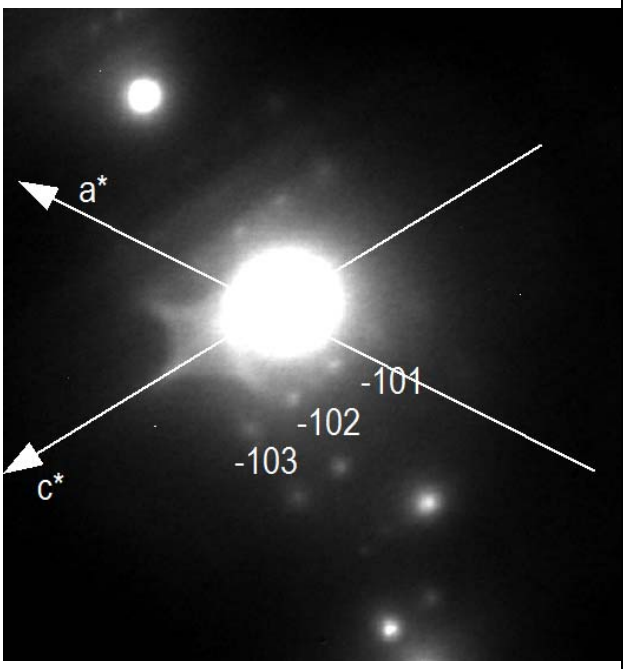

C

HkL	Dm	Ds	Dsd
-101	3.9	5.1	5.2
-102	4.85	4.1	4.0
-103	6.6	3.0	2.9

Figure DR5-2 **A:** SAED pattern of the Magneli phase Ti_5O_9; **B.** magnified image of the SAED pattern showing rows of diffraction spots parallel to c*; the small spacing between diffraction spots with the indices (h0l) and (0kl) is characteristic for SAED pattern of Magneli phases; selected diffraction spots were indexed on the basis of the cell setting given by Andersson (1960) Acta Chem. Scand. 14, 1161; **C.** Table with the indices of the diffraction spots shown in **B**, measured distances of diffraction spots to (000) (Dm), calculated (Ds) and recorded (Dsd) d-spacing for the diffraction spots; the spacing between the diffraction spots along c* is in this case d = 7.7Å in close agreement with the reported value of d=7.8 Å by Andersson (1960).

Table DR5-1. Diffraction data of all other phases: SAED pattern, measured distances (Dm) between diffraction spots and (000), calculated d-spacing (Ds), d-spacing listed in data bases (Dsd), indices and phases (I/P)

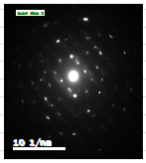

Ti4O7

Dm	Ds	Dsd	I/P
4.7	4.3	4.3	-102
4.8	4.2	4.3	-102
6.8	2.9	2.9	122
7.4	2.7	2.6	200
5.3	3.8	3.7	102
5.3	3.7	3.7	102
7.1	2.8	2.8	104
9.6	2.1	2.1	204
13.4	1.5	1.5	108

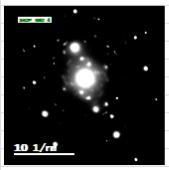

Ti4O7/goethite

Dm	Ds	Dsd	I/P
4.6	4.4	4.3	Ti4O7 102
3.4	6.0	6.1	Ti4O7 002
4.8	4.2	4.2	goethite 101
6.7	3.0	3.1	Ti4O7 004
11.1	1.8	1.8	Ti4O7 302
7.9	2.5	2.5	Ti4O7 200
3.8	5.2	5.2	Ti4O7 100
7.9	2.5	2.5	Ti4O7 104
11.2	1.8	1.8	Ti4O7 302

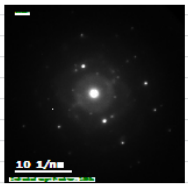

hematite

Dm	Ds	Dsd	I/P
7.6	2.6	2.7	104
7.3	2.7	2.7	104
10.6	1.9	1.8	204
10.5	1.9	1.8	204
10.7	1.9	1.8	204
10.8	1.9	1.8	204

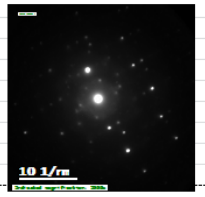

Ti4O7

Dm	Ds	Dsd	I/P
6.4	3.1	3.1	004
6.5	3.1	3.1	004
10.6	1.9	1.9	0-26
10.8	1.9	1.9	0-26
8.4	2.4	2.4	-222
6.3	3.2	3.1	0-22
4.7	4.2	4.3	102
6.4	3.1	3.12	0-22
10.8	1.9	1.9	0-26

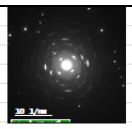

zircon

Dm	Ds	Dsd	I/P
4.5	4.5	4.4	101
9.0	2.2	2.2	202
6.0	3.3	3.3	200
9.5	2.1	2.1	301

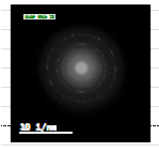

illite/smectite

Dm	Ds	Dsd	I/P
4.9	4.1	4.1	021
4.0	5.0	5.0	002
9.4	2.1	2.2	-133
7.4	2.7	2.7	023
6.6	3.0	3.1	112
12.9	1.5	1.5	-206

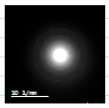

kaolinite

Dm	Ds	Dsd	I/P
5.7	3.5	3.6	004
9.9	2.0	2.0	134
2.8	7.1	7.2	002

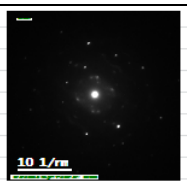

Ti4O7

Dm	Ds	Dsd	I/P
4.7	4.3	4.3	-102
6.5	3.1	3.0	1-22
6.7	3.0	3.1	004
4.7	4.2	4.3	-102
11.0	1.8	1.9	0-26
11.3	1.8	1.7	-302

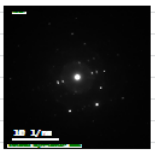

Ti4O7/goethite

Dm	Ds	Dsd	I/P
6.7	3.0	3.0	220 Ti4O7
8.8	2.3	2.3	200 goethite
6.5	3.1	3.0	220 Ti4O7
15.1	1.3	1.3	620 Ti4O7

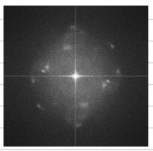

kleberite/anatase

Dm	Ds	Dsd	I/P
5.2	3.8	3.9	-111 kleberite
5.6	3.6	3.5	101 anatase
5.1	3.9	3.9	-111 kleberite
8.0	2.5	2.6	-113 kleberite
7.1	2.8	2.8	-211 kleberite

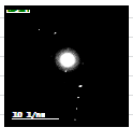

illite/smectite

Dm	Ds	Dsd	I/P
5.0	4.0	4.1	021
6.9	2.9	2.9	-113
4.0	5.0	5.0	002
5.2	3.9	3.8	111
2.8	7.0		

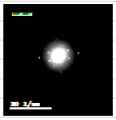

illite/smectite

Dm	Ds	Dsd	I/P
5.2	3.9	3.7	-112
9.5	2.1	2.0	005
5.0	4.0	4.1	021
7.7	2.6	2.7	023

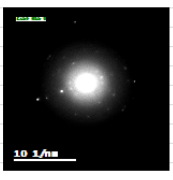

illite/smectite/hematite

Dm	Ds	Dsd	I/P
5.3	3.8	3.7	-112 illite/smectite
10.9	1.8	1.8	024 hematite
5.0	4.0	4.1	021 illite/smectite
7.7	2.6	2.7	023 illite/smectite
9.6	2.1	2.0	005 illite/smectite
13.5	1.5	1.5	060 illite/smectite

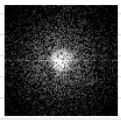

Ti4O7

Dm	Ds	Dsd	I/P
8.1	2.5	2.47	120
8.3	2.4	2.42	0-24
6.5	3.1	3.0	-122

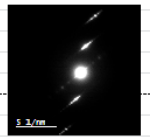

illite needles in Fe-Si matrix

Dm	Ds	Dsd	I/P
1.9	10.8	10.0	001
4.0	5.0	5.0	002
5.9	3.4	3.3	003
6.8	2.9	2.9	-113

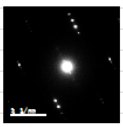

illite

Dm	Ds	Dsd	I/P
2.0	10.1	10.01	001

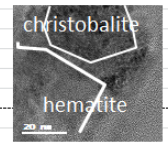

christobalite

Dm	Ds	Dsd	I/P
5.0	4.0	4.0	101
8.3	2.4	2.5	200

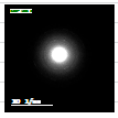

goethite

Dm	Ds	Dsd	I/P
7.3	2.7	2.7	301
12.7	1.6	1.6	511

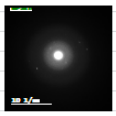

bernalite

Dm	Ds	Dsd	I/P
5.3	3.8	3.8	
6.8	2.9	?	
12.3	1.6	1.7	

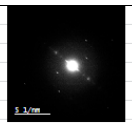

smectite close to feldspar

Dm	Ds	Dsd	I/P
1.9	10.6	10.01	001
5.8	3.4	3.3	003
4.0	5.0	5.0	002
4.6	4.4	4.3	111

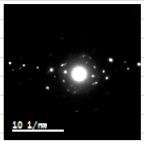

large hematite crystals

Dm	Ds	Dsd	I/P
5.4	3.7	3.7	012
10.8	1.9	1.8	024
6.6	3.0	3.0	220
13.4	1.5	1.5	440
5.3	3.8	3.7	012

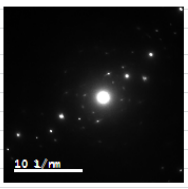

large hematite crystals

Dm	Ds	Dsd	I/P
13.7	1.5	1.5	300
5.3	3.8	3.7	012
10.8	1.8	1.8	024
5.5	3.6	3.7	012
7.8	2.6	2.5	110
10.9	1.8	1.8	024
9.5	2.1	2.1	022
13.6	1.5	1.5	300

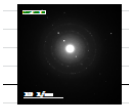

bernalite

Dm	Ds	Dsd	I/P
5.1	3.9	3.8	200
13.3	1.5	1.5	242
9.4	2.1	2.2	222

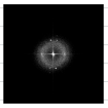

kaolinite/anatase/brookite/hematite

Dm	Ds	Dsd	I/P
4.4	4.5	4.4/4.5	kaolinite/illite
5.6	3.5	3.5	101/210 anatase/brookite
5.7	3.5	3.5	101/210 anatase/brookite
7.5	2.7	2.7	104 hematite

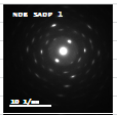

baddeleyite in Zr-Si rich area

Dm	Ds	Dsd	I/P
5.6	3.6	3.7	110
11.0	1.8	1.8	220
7.0	2.9	2.9	111
9.0	2.2	2.2	-211

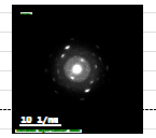

keldyshite NaZr[Si2O6OH

Dm	Ds	Dsd	I/P
5.0	4.0	4.0	200
11.8	1.7	1.7	-503
9.6	2.1	2.1	003
9.4	2.1	2.2	301
12.4	1.6	1.6	500

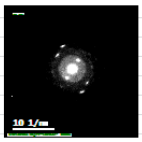

keldyshite/baddeleyite/zircon

Dm	Ds	Dsd	I/P
5.1	4.0	4.0	200 keldyshite
9.8	2.0	2.1	003 keldyshite
5.4	3.7	3.7	110 baddeleyite
12.1	1.7	1.7	503 keldyshite
8.0	2.5	2.5	220 zircon

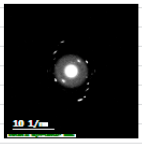

Zircon/keldyshite

Dm	Ds	Dsd	I/P
6.0	3.3	3.3	200 zircon
4.9	4.1	4.1	200 keldyshite
8.7	2.3	2.3	220 zircon
8.0	2.5	2.5	112 zircon
9.9	2.0	2.1	301 zircon
11.7	1.7	1.7	322 zircon

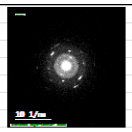

Zircon/keldyshite

Dm	Ds	Dsd	I/P
5.2	3.9	4.0	keldyshite
9.9	2.0	2.1	keldyshite
8.1	2.5	2.5	zircon
12.2	1.6	1.7	keldyshite
9.6	2.1	2.1	keldyshite

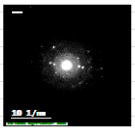

Ti4O7

Dm	Ds	Dsd	I/P
6.3	3.2	3.1	0-22
8.3	2.4	2.5	120
3.3	6.0	6.1	002
6.8	3.0	2.8	-104
8.3	2.4	2.4	0-24
11.4	1.8	1.8	-302